Author for correspondence:

Andrew Orkney

e-mail:

andrew.orkney@earth.ox.ac.uk

Bio-Optical evidence for increasing *Phaeocystis* dominance in the Barents Sea (Supplementary information)

http://dx.doi.org/10.1098/rsta.2019.0357

A. Orkney[1], T. Platt[2],

B.E. Narayanaswamy[3], I. Kostakis[4,5]

H.A. Bouman[1]

[1]Department of Earth Sciences, University of Oxford, 3 South Parks Road, Oxford OX1 3AN
[2]Plymouth Marine Laboratory, Prospect Place, Plymouth, PL1 3DH
[3] Scottish Association for Marine Science, Scottish Marine Institute, Oban, PA37 1QA
[4] School of Computing, University of Portsmouth, Portsmouth PO1 3HE, UK
[5] Physics Department, University of Strathclyde, Glasgow, G4 ONG, UK

We provide a detailed description of the structure and performance of the bio-optical algorithm we used to detect dominant phytoplankton groups in remotely sensed ocean-colour of the Barents Sea. The bio-optical algorithm can itself be de-constructed into 3 modules, which mask coccolithophore blooms, sediment and river plumes; recognise blooms of highly-packaged phytoplankton and finally distinguish between chlorophyll-c3-rich *Phaeocystis* blooms and chlorophyll-c3-poor diatom blooms. We then consider drift in the retrieval of the derived proxy of chlorophyll-c3 absorption signal and present time series of blooms identified in the Labrador and Barents Seas to supplement our submission.

THE ROYAL SOCIETY
PUBLISHING

1. Supplementary information

A modular flow chart of the structure of our Barents Sea Bio-Optical algorithm is presented in Figure 1.
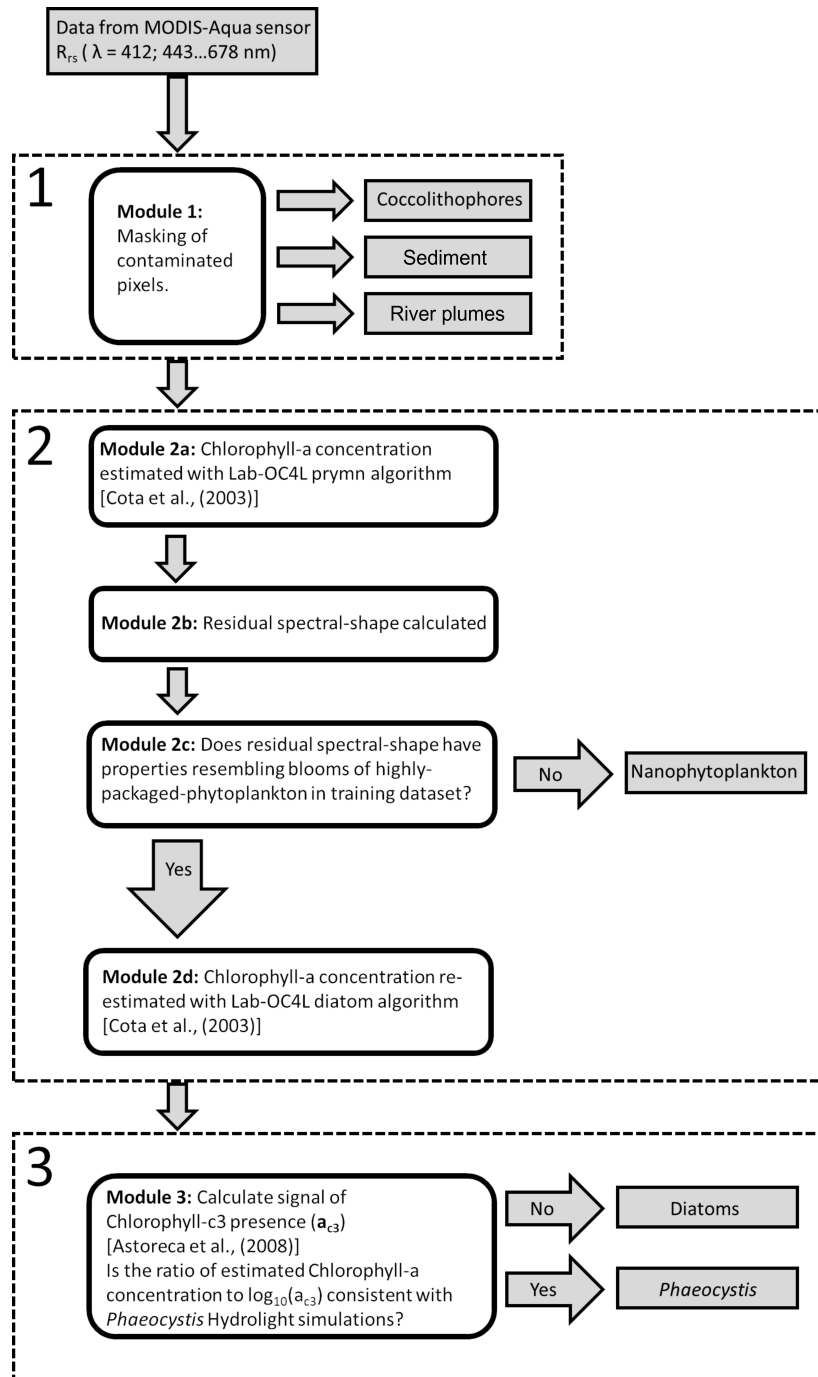

Figure 1. Modular flow chart of the structure of the Barents Sea bio-optical algorithm.

(a) Module 1: Masking contaminated pixels

We developed our bio-optical algorithm to discern different phytoplankton groups under the working assumption that the ratio of water-leaving radiance to down-welling irradiance (R_{rs}), is determined principally by elastic scattering (R^E). Elastic scattering is itself a wavelength-dependent (λ) function of absorption (a) and backscattering (b_b):

$$R^E(\lambda, 0) = r \frac{b_b(\lambda)}{a(\lambda) + b_b(\lambda)}, \tag{1.1}$$

where r is a coefficient of proportionality that varies with factors like the angle of incident light and the viewing angle.

The overall contribution of absorption by pure water, phytoplankton and CDOM to total absorption is additive;

$$a(\lambda) = a_w(\lambda) + a_{ph}(\lambda) + a_{cdom}(\lambda). \tag{1.2}$$

By assessing spectral shape- the wavelength dependent variation in R_{rs}, we avoid the requirement to consider variation in r (assuming it does not vary with wavelength), and we make the assumption that variation in a and b_b are driven principally by variation in phytoplankton taxonomic composition and pigment biomass. We take $a_w(\lambda)$ to be unchanging and previous research has shown that, in the open waters of the Barents Sea, $a_{cdom}(\lambda)$ (absorption due to Coloured Dissolved Organic Matter (CDOM)) is invariant across seasons and major hydrographic features and can therefore be treated as constant [1], with an absorption coefficient of $0.04\,\mathrm{m}^{-1}$ at 400 nm, decaying according to the relationship found in *Bricaud et al., (1981)* [2];

$$a_{cdom}(\lambda) = 0.04e^{(-0.0014(\lambda - 440))} \tag{1.3}$$

Hence, as the spectrum of $a_{cdom}(\lambda)$ is constant, we assume that change in $a(\lambda)$ is driven by change in $a_{ph}(\lambda)$ (phytoplankton absorption).

These assumptions are, however, violated when non-algal particles, which have their own strong absorption [3] and backscattering properties [4], are present in substantial concentrations. River plumes can also carry terrigenous organic matter, increasing $a_{cdom}(\lambda)$, and therefore violating our assumptions [5].

We therefore needed a means by which to identify ocean-colour observations in which our assumption that variation in spectral shape is driven by phytoplankton absorption is violated, so that we could mask them from consideration, which includes masking observations where coccolithophore blooms control spectral shape, because the heightened backscattering of light off of their biomineral liths greatly changes ocean-colour [6].

Module 1 (Figure 1) is the first of the stack of three stages that together constitute our bio-optical algorithm. We performed a Principal Component Analysis (PCA) to explore variation in ocean-colour R_{rs} measurements taken from the Barents Sea between 0 and 80 degrees East and 0 and 85 degrees North, in July 2014. We selected this region and time because coccolithophore blooms have been reported [7]. The geographic range of our sample also included the Ob River plume [5] and sediment-dominated fjords of the Svalbard archipelago [4]. We identified the geographic regions corresponding to these groups and created linear discriminants that distinguish these spectra from those of the open-ocean, where our assumptions can reasonably be expected to hold true. PC1-2 space spreads the dataset out into a central Gaussian distribution with 3 aberrant tails, corresponding to coccolithophores, river plumes and waters rich in fjordic sediments (Figure 2).

Figure 2. a) A Principal Component Analysis of ocean-colour in the Barents Sea, July 2014; blue, yellow, orange and cyan points correspond to normal ocean, river plumes, sediment and coccolithophores. The pink, dashed; green, dotted and brown solid lines correspond to the linear trends associated with river plumes, sediment and coccolithophores; linear discriminants were defined to bisect the angles between them. b) The red, dashed line represents the division between open-ocean ocean-colour and those masked as river plumes, sediment or coccolithophores. c) A map of the classifications, showing coherent geographic domains.

Module 1 takes acquired ocean-colour observations, projects them into the PCA space (Figure 2a) and uses the linear discriminants we previously defined to mask sediment-rich waters, river plumes and coccolithophore blooms. Only unmasked observations are then passed on to Module 2 of our bio-optical algorithm (Figure 1). Figure 3 demonstrates Module 1 effectively recognising and masking several coccolithophore blooms identified by the NASA Earth Observatory [8–10].
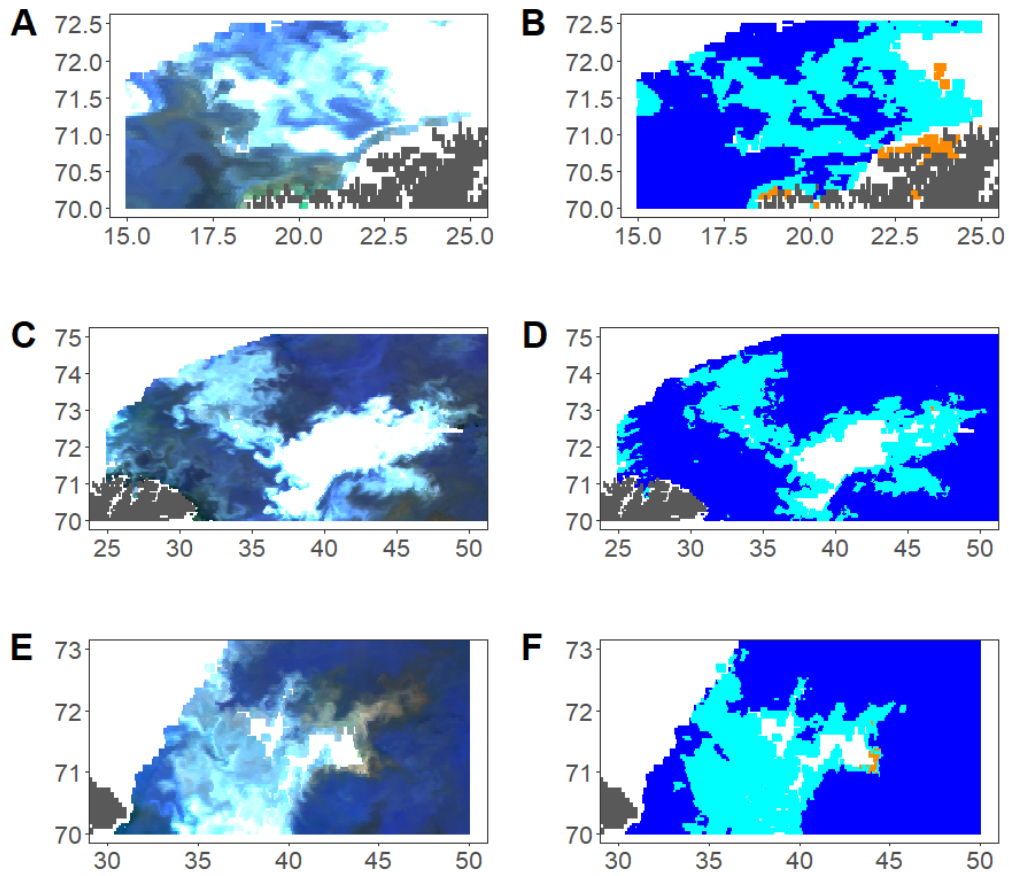
Figure 3. Examples of true colour images of coccolithophore blooms on the 24th of July 2003, 6th of July 2016 and 18th of July 2018 (A,C,E) and corresponding coccolithophore masks (B,D,F). Normal ocean is masked blue, coccolithophores are masked cyan and sediment is masked orange.

(b) Module 2: Discrimination of diatoms and *Phaeocystis* from nanophytoplankton

Module 2 (Figure 1) distinguishes blooms of highly-packaged phytoplankton (diatoms and the colonial prymnesiophyte *Phaeocystis*), from populations of unicellular nanophytoplankton. We adopt the term 'nanophytoplankton' here to describe a subset of those populations referred to as 'prymnesiophyte' in *Stuart et al., (2000)* and *Cota et al., (2003)* [11,12]. Nanophytoplankton identified in the Labrador Sea by *Stuart et al., (2000)* and *Cota et al., (2003)* are optically distinct from *Phaeocystis*, with a much lower degree of pigment-packaging. Given that *Phaeocystis* is a type of prymnesiophyte, we believe the term 'nanophytoplankton', is more useful for our purposes. We present the relationship between the system of terms we use here in Figure 5. Module 2 was constructed empirically; a training dataset of diatom, dinoflagellate, *Phaeocystis* and nanophytoplankton ocean-colour observations was constructed with reference to samples of phytoplankton collected in the Barents Sea between June 2017 and July 2018 (Sampling locations displayed in Figure 4).
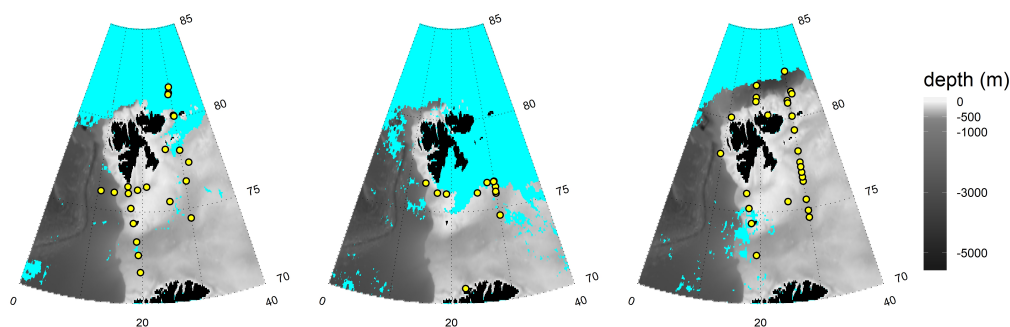

Figure 4. Left: Map of phytoplankton sampling sites on cruise JR16006 (Julian days 189-217), Centre: Map of phytoplankton sampling sites on cruise HH23042018 (Julian days 114-122), Right: Map of phytoplankton sampling sites on cruise JR17006 (Julian days 163-185). Regions with no concomitant MODIS-Aqua ocean-colour observations during the cruise window are masked in cyan, providing a general indication of the sea ice edge.

Distinct phytoplankton assemblages dominating in-situ samples were recognised by their absorptive properties. We followed the protocol of *Stuart et al., (2000)* [11] to record phytoplankton absorption spectra, including their pigment extraction methods and choice of path-length correction. In total, 191 Barents absorption spectra are presented in this study.

We chose to match our method to *Stuart et al., (2000)* so that we could pool our Barents dataset with a similar dataset of $a_{ph}(\lambda)$ collected in the Labrador Sea [11–13], in which diatom and *Phaeocystis*-dominated blooms had also been sampled. The Labrador Sea dataset was collected between 1996 and 2001 in multiple seasons. Comparing $a_{ph}(\lambda)$ in the Barents and Labrador Seas therefore allowed us to gain greater confidence that any recognition of distinct bio-optical assemblages common to both Seas is robust to seasonal and inter-annual variation. We then decomposed the $a_{ph}(\lambda)$ associated with our phytoplankton samples, and those of *Stuart et al., (2000)* into Gaussian functions that represent the contribution from different suites of phytoplankton pigments to absorption, following the method of *Chase et al., (2013)* (itself a

formalisation of earlier schemes employed by *Hoeppfner and Sathyendranath, (1993)* and *Lohrenz et al., (2003)* [14–16]). This approach reduced the number of variables and made the dataset more tractable. *Liu et al., (2019)* have previously demonstrated the efficacy of this method in summarising variability in $a_{ph}(\lambda)$, by relating decomposed $a_{ph}(\lambda)$ to concentrations of taxonomically-indicative pigments measured with High Performance Liquid Chromatography (HPLC) in the western Barents Sea [17]. The Labrador Sea phytoplankton samples had already been prescribed likely identities as diatom or nanophytoplankton dominated, based on HPLC [11], but we added a third category, classifying those blooms rich in chlorophyll-c3 as *Phaeocystis*, which commonly occur off the Greenland Shelf [12,18]. Using a combination of optical microscopy, HPLC and PCA performed on the decomposed $a_{ph}(\lambda)$, we recognised that the Barents phytoplankton samples we collected could be divided into 4 distinct bio-optical communities dominated by nanophytoplankton, colonial *Phaeocystis*, diatoms and dinoflagellates (Figure 5). It can be seen in Figure 5 that *Phaeocystis* is optically distinct from nanophytoplankton– exhibiting a much greater degree of pigment-packaging and having a greater resemblance to the diatoms; a shoulder in $a_{ph}(\lambda)$ around 469 nm distinguishes *Phaeocystis* from diatoms. This feature probably results from absorption due to chlorophyll-c3.
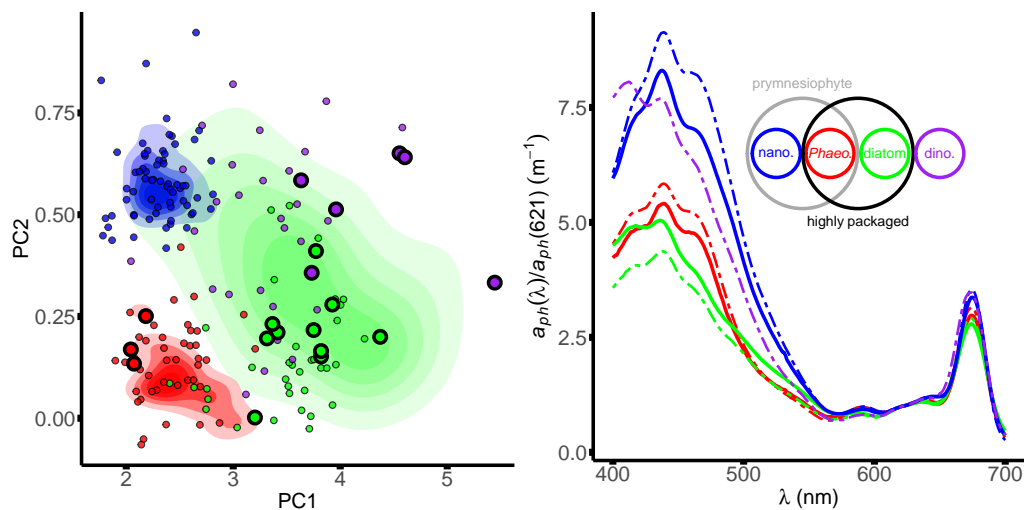

Figure 5. Left: A PCA space representing variation in the optical properties of the Barents phytoplankton samples. The density gradients represent the regions of this space occupied by nanophytoplankton, diatom and *Phaeocystis* samples identified in the Labrador Sea (blue, green, red). The bold points represent a sub-set of Barents Sea phytoplankton which optical microscopy showed to be dominated exclusively by *Phaeocystis*, diatoms or dinoflagellates (red, green, purple), while the smaller points represent the rest of the Barents phytoplankton samples after a fuzzy clustering algorithm was instructed to divide them into four groups. Right: Representative average absorption spectra for nanophytoplankton, dinoflagellates, *Phaeocystis* and diatoms (blue, purple, green, red) for the Labrador (bold) and Barents (dashed) Sea datasets, showing high similarity.

We then took the date of sampling and geographic locations of our in-situ Barents samples and collected all available daily MODIA-Aqua ocean-colour observations [19] within 1 degree latitude or longitude; 18,000 observations in total. Module 1 was used to exclude observations contaminated by coccolithophores, sediments or river plumes. The remaining observations were then deposited into a training dataset of ≈16,000 ocean-colour observations. We labelled the observations in the training dataset, according to the inferred phytoplankton group (Figure 5) of the in-situ sample they were associated with.

Variation in the ocean-colour spectral shape is primarily driven by variations *chl-a* rather than

variation between different phytoplankton assemblages, potentially obscuring patterns of ocean-colour that might distinguish different bio-optical assemblages of phytoplankton. We followed a similar method to *Alvain et al., (2008)* [20] in order to remove the confounding effects of *chl-a* on ocean-colour. We constructed a regression of ocean-colour in all diatom-labelled entries in our database against the *chl-a* concentration inferred from them with the **Lab-OC4L diatom** *chl-a* algorithm of *Cota et al., (2003)*. We then subtracted the predicted spectra from the MODIS-Aqua ocean-colour observations in our training database, to arrive at 'residual' ocean-colour, in which the remaining variance should correspond to variation in phytoplankton assemblage and not simply *chl-a* concentration. In order to be especially conservative, we decided to estimate the *chl-a* concentration of all ocean-colour observations that we hope to classify in accordance with the **Lab-OC4L prymn** *chl-a* algorithm published by *Cota et al., 2003* [12], which generally predicts higher values than **Lab-OC4L diatom**. This has the effect of decreasing bias to conflate change in *chl-a* with change in phytoplankton groups.

We then used 1000 permutations of hold-p-out cross validation, with p set to 500, to build linear discriminant analyses and test whether we could consistently use the held-in ocean-colour observations to classify the held-out ocean-colour observations in our training dataset. We found that diatoms and *Phaeocystis* could reliably be distinguished from nanophytoplankton (3% and 20% of diatom and *Phaeocystis*-labelled entries are classified as nanophytoplankton, respectively), but that diatoms and *Phaeocystis* were often misclassified (53% of *Phaeocystis*-labelled entries were classified as diatoms) . We found it difficult to consistently recognise dinoflagellates. While 57% of dinoflagellate-labelled entries were correctly identified, we suspected this was because they tended to occur in oligotrophic waters– and that their identification was more a function of a residual signal of *chl-a* content and not of assemblage-specific phytoplankton optical properties. Some 68% of nanophytoplankton-labelled entries were correctly recognised.

This capacity for consistent classification of our training dataset compared favourably with existing algorithms that discern diatoms from nanophytoplankton, developed by *Sathyendranath et al., 2004* [13] and *Jackson et al., 2010* [21]. We tested these two algorithms by adapting them to use the nearest available MODIS-Aqua wavebands. When we used the two diatom-detection algorithms to classify spectra in our training dataset they tended to have a bias in favour of diatoms (only 40 and 42% of nanophytoplankton-labelled entries in our dataset were correctly classified, respectively).

(c) Module 3: Discrimination of diatom and *Phaeocystis* blooms

Given our weaker confidence in the detection of dinoflagellate blooms, we made the decision to exclude dinoflagellate-labelled entries from our training dataset and to concentrate on the utility of the linear discriminant we had found for distinguishing blooms of highly-packaged phytoplankton (diatoms and *Phaeocystis*) from ocean waters dominated by nanophytoplankton. Owing to the optical similarity of diatom and *Phaeocystis*-labelled ocean-colour residual spectral shape, we considered the possibility that the differences between diatom and *Phaeocystis* ocean-colour observations are subtle and that our linear discriminant analysis had not found them. We therefore opted to develop a third algorithm module, with the intent to take ocean-colour residual spectra labelled as highly-packaged phytoplankton and divide them into diatom and *Phaeocystis* dominated measurements.

Module 3 (Figure 1) is a semi-empirical algorithm. We made use of Hydrolight-Ecolight software [22] to simulate the expected ocean-colour under conditions of diatom and *Phaeocystis* dominance, for *chl-a* concentrations ranging between 0.1 and 25 mg m^{-3} (measured values of in-situ samples varied between 0.11 and 24.23 mg m^{-3}). We implemented these simulations with phytoplankton absorption spectra for our diatom and *Phaeocystis* groups (as in Figure 5), a chlorophyll-specific scattering model based on a combination of Barents and Liqurian Sea measurements and a chlorophyll-specific back-scattering model based on a combination of Barents Sea and

NOMAD measurements [23]. The spectral absorption of phytoplankton was constrained to evolve according to the relationship identified in *Bricaud et al., (1995)* [24] and absorption due to CDOM was treated as constant, with a value of $0.04\,\mathrm{m}^{-1}$ at 440 nm [1], decaying with wavelength according to the function identified by *Bricaud et al., (1981)* [2]. Scattering and back-scattering model coefficients are presented in Table 1, wherein scattering and back-scattering evolve according to equation 1.4:

$$b_i(\lambda) = A_i(\lambda)(chl\text{-}a)^{B_i(\lambda)}, \tag{1.4}$$

where b_1 represents total scattering of particles and seawater (m^{-1}), b_2 represents backscattering (m^{-1}); *chl-a* is the chlorophyll-a concentration $(\mathrm{mg\,m}^{-3})$, and A_i and B_i represent fit parameters.

Table 1. Scattering and Backscattering model coefficients and goodness of fit.

λ (nm)	A_1	B_1	R_1^2	A_2	B_2	R_2^2
412	0.3893	0.0842	0.0177	0.0027	0.4116	0.5727
440	0.4235	0.4089	0.2606	0.0026	0.4967	0.7643
488	0.4271	0.4282	0.2814	0.0023	0.5017	0.7614
510	0.4324	0.4403	0.2961	0.0022	0.5038	0.7581
532	0.4418	0.4852	0.4803	0.0021	0.4898	0.7503
555	0.4459	0.5105	0.5071	0.0020	0.5033	0.7453
650	0.3972	0.4554	0.2833	0.0016	0.5169	0.7132
676	0.3777	0.5215	0.4662	0.0015	0.5048	0.7016
712	0.3595	0.1879	0.0884	no NOMAD data		

We recognise that *Phaeocystis* is a chlorophyll-c3-rich plankton, compared with diatoms, and therefore surmised that we might be able exploit this optical difference– evident in Figure 5– in order to distinguish between our simulated spectra, and then evaluate whether it is possible to distinguish diatom and *Phaeocystis* blooms in our training dataset. We adopted the chlorophyll-c3 absorption algorithm developed by *Astoreca et al., (2008)* [25] to determine whether a signal attributable to chlorophyll-c3 could be detected in the diatom and *Phaeocystis* Hydrolight simulations, and made use of the **Lab-OC4L diatom** *chl-a* algorithm published by *Cota et al., (2003)* [12] to infer *chl-a* content, reasoning that *Phaeocystis* would be typified by a high chlorophyll-c3 signal per unit biomass, compared to diatoms. The chlorophyll-c3 algorithm of *Astoreca et a., (2008)* relies upon use of the MODIS land band centred at 469 nm to detect a shoulder in $a_{ph}(\lambda)$ associated with chlorophyll-c3 (consult Figure 5 to observe this feature). The use of the MODIS land bands, including 469 nm, has already been applied to the identification of bio-optically distinct phytoplankton blooms by *Hu et al., (2010)* [26], who successfully identified *Trichodesmium* blooms in optically complex coastal waters. We found *chl-a* estimates were broadly lower than expected (Figure 6), however given that the magnitude of simulated absorption spectra used as input to Hydrolight are computed as a function of *chl-a* we should still expect the relationship between absorption signal attributable to chlorophyll-c3 and *chl-a* to be informative. We found, upon performing a PCA on ocean-colour residual spectra in our training database labelled as diatom or *Phaeocystis*, that there was a bimodal normal distribution of the data in Principal Component 5-6 space (Figure 6 a,d). We suspected that this likely represented two dominating phytoplankton assemblages, but we note that the entries labelled as diatom or *Phaeocystis* are distributed across both of the Gaussian features, suggesting that the reason that linear discriminant analysis could not retrieve an effective discriminant was due to labelling in the training dataset confusing these groups– probably as a result of their close spatial co-occurrence during cruises. It is clear that the relationship between *chl-a* and the common logarithm of absorption signal attributable to chlorophyll-c3 ($log_{10}(a_{c3})$) separates diatom and *Phaeocystis* from one another in Hydrolight simulations (Figure 6 c). We derived a linear discriminant relating
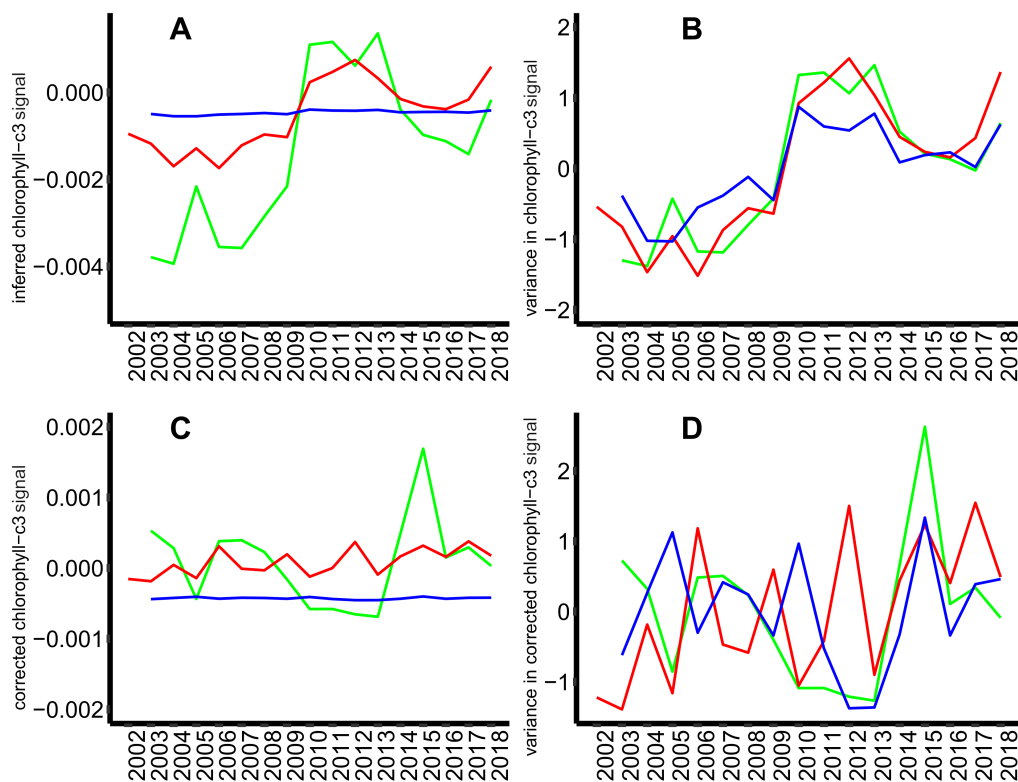
$log_{10}(a_{c3})$ and inferred *chl-a* concentration to divide diatom and *Phaeocystis* simulations. When this was applied to the training dataset, the results broadly conformed to the two Gaussian features we had previously identified (Figure 6 b).

Figure 6. A) PC5-6 rotation of the training entries for diatoms (light blue) and *Phaeocystis* (dark blue)– point size is scaled to inferred *chl-a* concentration. B) The same space as A except entries have been re-classified in accordance our bio-optical algorithm; diatoms (green), *Phaeocystis* (magenta), nanophytoplankton (blue). C) a linear discriminant is developed that distinguishes simulated diatoms (black) from simulated *Phaeocystis* (dark red), with the training dataset entries from B projected onto the space. D) A histogram, illustrating bimodal distribution of training dataset entries along PC5.

Figure 7. A) Annually-binned mean signal due to chlorophyll-c3 for the Labrador (green), Barents (red) and North-Atlantic Sub-Tropical Gyre (blue). B) Trends in inferred chlorophyll-c3 signal normalised to variance, with Sub-Tropical Gyre variance multiplied by 10 to make it visible. C) Annually-binned mean signal due to chlorophyll-c3 after a correction for drift is applied. D) Trends in corrected chlorophyll-c3 signal normalised to variance, with Sub-Tropical Gyre variance multiplied by 10 to make it perceptible.

We now move on to discuss the stability of the derived variable, chlorophyll-c3 absorption signal (a_{c3}), in time series of MODIS-Aqua ocean-colour. We assessed this by compiling time series of mean a_{c3} estimated from ocean-colour across several years in different parts of the global ocean that we would not expect to behave in unison. If these disparate regions show common changes it may provide evidence of systematic bias in the inference of a_{c3}. We chose to investigate the North Atlantic Sub-Tropical Gyre in particular because we should expect the ocean-colour in the region to be relatively constant over time, as it is oligotrophic (*chl-a* <0.1 mg m^{-3}), and to a first-order may be presumed to represent clear ocean waters when contrasted with the eutrophic Barents or Labrador Seas (which we define as the regions between 70-85 degrees North, 0-50 degrees East and 50-65 degrees North, 40 to 60 degrees West) .

In Figure 7 the North Atlantic Sub-Tropical Gyre region is assumed to occupy the region between 30-50 degrees West and 25-35 degrees North. We downloaded MODIS-Aqua ocean-colour observations in this region for Julian days 130-135 between 2003-2018. The fact that a_{c3} in this region is clearly related to that in the Barents and Labrador Seas (Figure 7 b) evidences drift in the representation of ocean-colour from the MODIS-Aqua r2018.1 reprocessing; a clear step-change is visible in all time series at 2010, for example. It is hence necessary to correct for this systemic form of bias. Our correction scheme is based on that of *Taylor et al.,* [27], who observed

a shift in the spectral output of the IASI (Infrared Atmospheric Sounding Interferometer) remote-sensing platform in 2010, which biased results in an algorithm they had developed to infer sulphur dioxide. To correct for this drift *Taylor et al.*, took the lowest concentration of inferred sulphur dioxide in any image, that was within 1 standard deviation of the mean, and added its magnitude to all remaining pixels. In our approach we first constrained all a_{c3} signal values to within -0.01 and 0.005 (see Figure 7 a), so that aberrant values would not significantly disturb calculation of the standard deviation. The lower negative limit of -0.01 may be surprising, but *Astoreca et al., (2008)* [25] themselves found that inferred a_{c3} signal became negative in diatom-dominated conditions. We then divided the values into an annually-binned time series and calculated the difference between the mean annual a_{c3} values and the lowest a_{c3} value in each annual bin that fell within 1 standard deviation of the mean a_{c3} in each bin. We added the magnitude of the lowest annually-binned a_{c3} values to the remaining a_{c3} values in each bin, and then shifted the resulting absorption values so that the mean of all a_{c3} values between 2010-2018 matched the mean of the original a_{c3} values (since our bio-optical algorithm was constructed around in-situ samples collected after the 2010 shift in inferred chlorophyll-c3 absorption). In our efforts to illustrate drift in sensor output we computed pair-wise t-tests comparing mean R_{rs} values between 2003-2009 and 2010-2018 in the North Atlantic Sub-Tropical Gyre (Figure 8). We found that a significant shift has occurred among the most blue bands and that this was associated with an decrease in the R_{rs} of bands with the shortest wavelengths. *Astoreca et al., (2008)* had speculated on the question of whether minute differences in R_{rs} near 469 nm would be perceptible by remote-sensing platforms. We believe we have found evidence that these differences are detectable (Figure 6), but we caution that for the particular application of distinguishing *Phaeocystis* from diatom blooms, it appears necessary to account for anomalies resulting from temporal drift. We caution that different correction schemes may be necessary for future ocean-colour reprocessings, because they may subtly alter the ratios between different ocean-colour wavebands in a systematic fashion. After a correction scheme is applied, it can be seen that temporal drift in mean annualy-binned a_{c3} is largely removed and patterns of variance in the different seas can be considered decoupled (Figure 7).
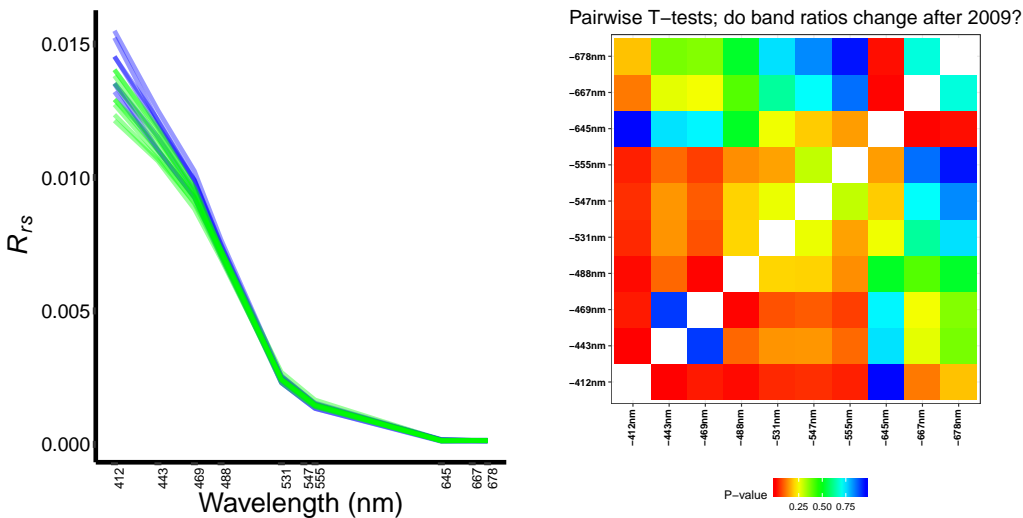

Figure 8. Left: Ocean-colour reflectance spectra for the North Atlantic Sub-Tropical Gyre before 2010 (blue) and after 2010 (green), a shift in spectral shape is evident. Right: Pair-wise tests for separation of means show that band ratios among the bands 443, 469 and 488nm have shifted significantly after 2010.

Figures 9 and 10 represent time series for the occurrence of different phytoplankton blooms, identified with our experimental bio-optical algorithm, in the Labrador and Barents Seas, once the correction for drift is applied. These figures are intended to be used as an adjunct to aid interpretation of the main text. Figure 9 is a validation exercise, comparing our experimental bio-optical algorithm classifications with an inter-annual time series of phytoplankton assemblages presented in [18].
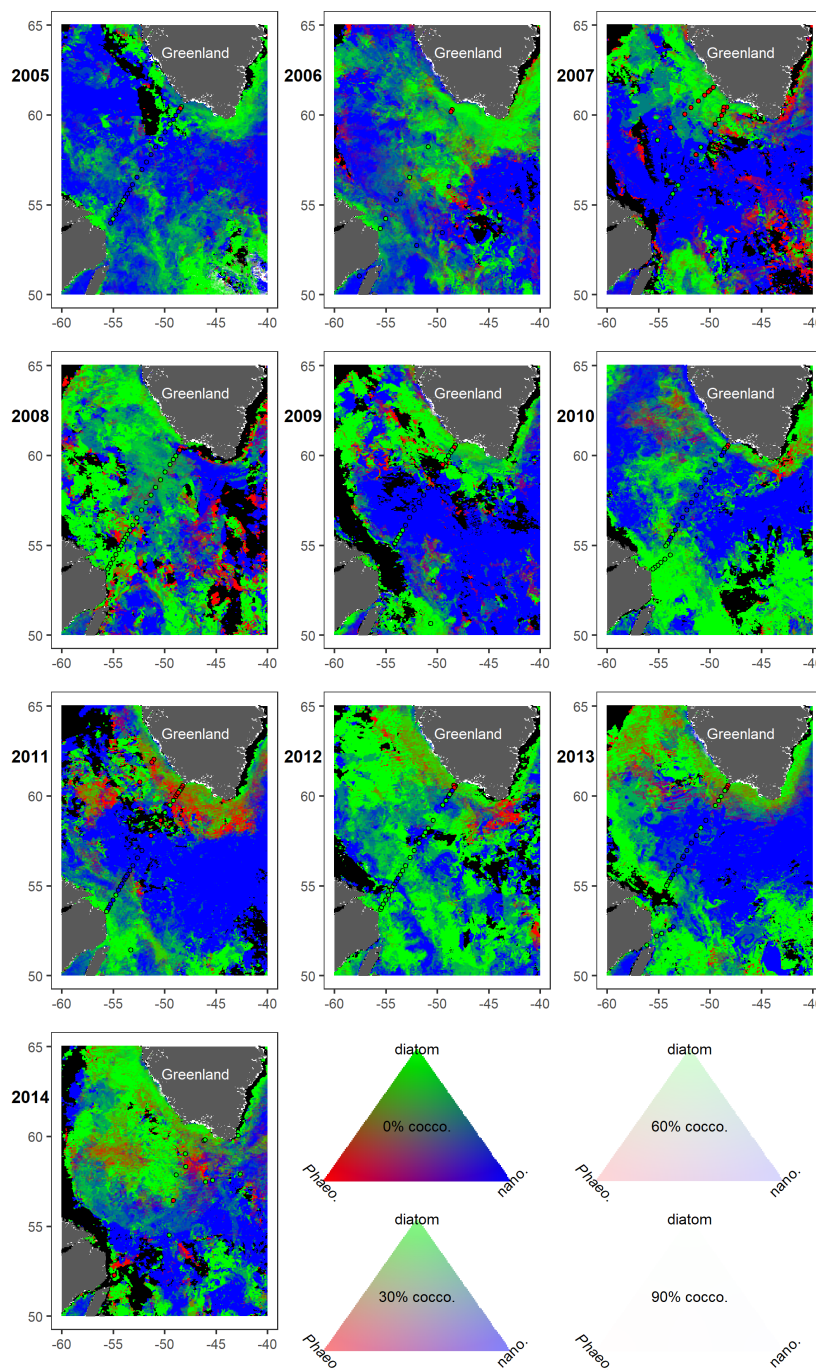
Figure 9. Phytoplankton blooms retrieved by remote-sensing in the Labrador Sea (background colour). Colour indicates frequency of phytoplankton classifications; red pixels indicate *Phaeocystis* dominance, green pixels indicate diatom dominance and blue pixels indicate nanophytoplankton dominance. White pixels are dominated by coccolithophores. This colourfield can be envisaged as a triangular prism with red, green and blue vertices, increasing in luminosity along its length. Slices of the colour field are presented as a visual key. Black pixels represent regions with no observations in a given year. The background is over-lain with in-situ samples taken by *Fragoso et al., 2017* [18] (circular dots: dataset accessible at https://doi.pangaea.de/10.1594/PANGAEA.871872). Red-filled circles represent *Phaeocystis*-rich samples, green-filled circles represent diatom-dominated samples and blue-filled circles represent mixed populations dominated by nanophytoplankton.
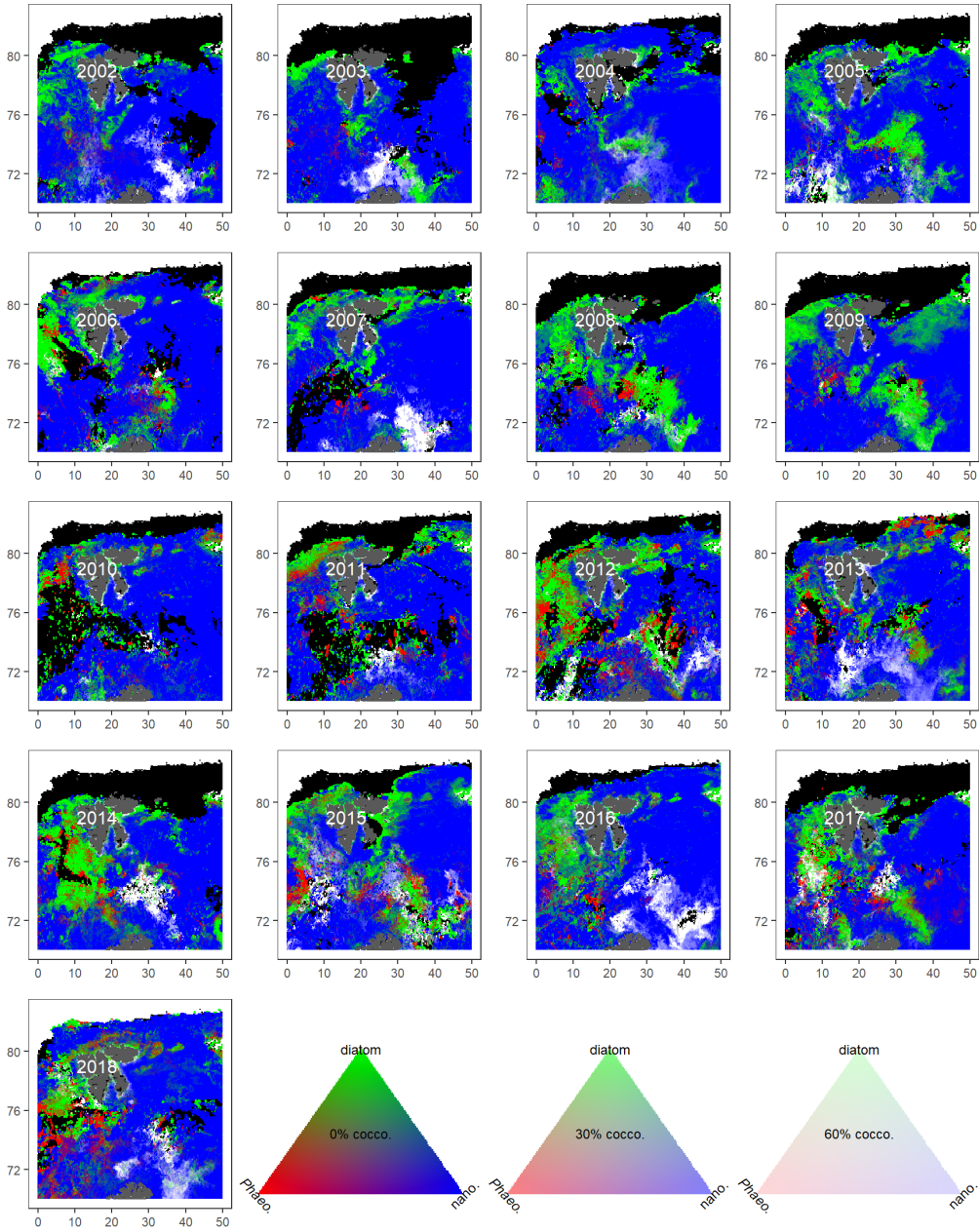
Figure 10. Phytoplankton blooms retrieved by remote-sensing in the Barents sea. Colour indicates frequency of phytoplankton classifications; red pixels indicate *Phaeocystis* dominance, green pixels indicate diatom dominance and blue pixels indicate nanophytoplankton dominance. White pixels are dominated by coccolithophores. This colourfield can be envisaged as a triangular prism with red, green and blue vertices, increasing in luminosity along its length. Slices of the colour field are presented as a visual key. Black pixels represent regions with no observations in a given year.

References

1. Hancke K, Hovland EK, Volent Z, Pettersen R, Johnsen G, Moline M, et al.
   Optical properties of CDOM across the Polar Front in the Barents Sea: Origin, distribution and significance.
   Journal of Marine Systems. 2014;130:219–227.
2. Bricaud A, Morel A, Prieur L.
   Absorption by dissolved organic matter of the sea (yellow substance) in the UV and visible domains1.
   Limnology and Oceanography. 1981;26(1):43–53.
3. Babin M, Stramski D, Ferrari GM, Claustre H, Bricaud A, Obolensky G, et al.
   Variations in the light absorption coefficients of phytoplankton, nonalgal particles, and dissolved organic matter in coastal waters around Europe.
   Journal of Geophysical Research: Oceans. 2003;108(C7).
4. Meslard F, Bourrin F, Many G, Kerhervé P.
   Suspended particle dynamics and fluxes in an Arctic fjord (Kongsfjorden, Svalbard).
   Estuarine, Coastal and Shelf Science. 2018;204:212–224.
5. Drozdova A, Patsaeva S, Khundzhua D.
   Fluorescence of dissolved organic matter as a marker for distribution of desalinated waters in the Kara Sea and bays of Novaya Zemlya archipelago.
   Oceanology. 2017;57(1):41–47.
6. Hovland EK, Dierssen HM, Ferreira AS, Johnsen G.
   Dynamics regulating major trends in Barents Sea temperatures and subsequent effect on remotely sensed particulate inorganic carbon.
   Marine Ecology Progress Series. 2013;484:17–32.
7. Carlowicz M, Norman K, Signorini S.
   Dueling Blooms NASA Earth Observatory. 2014.
   Accessed: 2019-04-17.
   Available from: https://earthobservatory.nasa.gov/images/84135/dueling-blooms.
8. GSFC MRRTN.
   Spectacular Bloom in the Barents Sea. 2003.
   Accessed: 2020-03-03.
   Available from: https://earthobservatory.nasa.gov/images/3649/spectacular-bloom-in-the-barents-sea.

9. Hansen K, Schmaltz J, Stevens J.
   The Barents Sea Abloom. 2016.
   Accessed: 2020-03-03.
   Available from: https://earthobservatory.nasa.gov/images/88316/the-barents-sea-abloom.

10. Carlowicz M, Stevens J, Dauphin L.
    Summer Blooms in the Baltic and Barents. 2018.
    Accessed: 2020-03-03.
    Available from: https://earthobservatory.nasa.gov/images/92462/summer-blooms-in-the-baltic-and-barents.

11. Stuart V, Sathyendranath S, Head E, Platt T, Irwin B, Maass H.
    Bio-optical characteristics of diatom and prymnesiophyte populations in the Labrador Sea.
    Marine Ecology Progress Series. 2000;201:91–106.

12. Cota GF, Harrison WG, Platt T, Sathyendranath S, Stuart V.
    Bio-optical properties of the Labrador Sea.
    Journal of Geophysical Research: Oceans. 2003;108(C7).

13. Sathyendranath S, Watts L, Devred E, Platt T, Caverhill C, Maass H.
    Discrimination of diatoms from other phytoplankton using ocean-colour data.
    Marine Ecology Progress Series. 2004;272:59–68.

14. Chase A, Boss E, Zaneveld R, Bricaud A, Claustre H, Ras J, et al.
    Decomposition of in situ particulate absorption spectra.
    Methods in Oceanography. 2013;7:110–124.

15. Hoepffner N, Sathyendranath S.
    Determination of the major groups of phytoplankton pigments from the absorption spectra of total particulate matter.
    Journal of Geophysical Research: Oceans. 1993;98(C12):22789–22803.

16. Lohrenz SE, Weidemann AD, Tuel M.
    Phytoplankton spectral absorption as influenced by community size structure and pigment composition.
    Journal of Plankton Research. 2003;25(1):35–61.

17. Liu Y, Boss E, Chase A, Xi H, Zhang X, Röttgers R, et al.
    Retrieval of phytoplankton pigments from underway spectrophotometry in the Fram Strait.
    Remote Sensing. 2019;11(3):318.

18. Fragoso GM, Poulton AJ, Yashayaev IM, Head EJ, Purdie DA.
    Spring phytoplankton communities of the Labrador Sea (2005–2014): pigment signatures, photophysiology and elemental ratios.
    Biogeosciences. 2017;14:1235–1259.

19. OBPG.
    Moderate-resolution Imaging Spectroradiometer (MODIS) Aqua Daily L3SMI Ocean Colour Data.
    NASA Goddard Space Flight Center, Ocean Ecology Laboratory, Ocean Biology Processing Group Moderate-resolution Imaging Spectroradiometer (MODIS) Aqua Daily L3SMI Ocean Colour Data Data; NASA OBDAAC, Greenbelt, MD, USA. 2019.

20. Alvain S, Moulin C, Dandonneau Y, Loisel H.
    Seasonal distribution and succession of dominant phytoplankton groups in the Global Ocean: A satellite view.
    Global Biogeochemical Cycles. 2008;22(3).

21. Jackson T, Bouman HA, Sathyendranath S, Devred E.
    Regional-scale changes in diatom distribution in the Humboldt upwelling system as revealed by remote sensing: implications for fisheries.
    ICES Journal of Marine Science. 2010;68(4):729–736.

22. Mobley C, Sundman L.
    HydroLight 5.1 EcoLight 5.1 Users' Guide, Sequoia Scientific.
    Inc, Bellevue. 2012.

23. Valente A, Sathyendranath S, Brotas V, Groom S, Grant M, Taberner M, et al.
    A compilation of global bio-optical in situ data for ocean-colour satellite applications–version two.
    Earth System Science Data. 2019;11(3):1037–1068.

24. Bricaud A, Babin M, Morel A, Claustre H.
    Variability in the chlorophyll-specific absorption coefficients of natural phytoplankton: Analysis and parameterization.
    Journal of Geophysical Research: Oceans. 1995;100(C7):13321–13332.

25. Astoreca R, Rousseau V, Ruddick K, Knechciak C, Van Mol B, Parent JY, et al.
    Development and application of an algorithm for detecting *Phaeocystis globosa* blooms in the Case 2 Southern North Sea waters.
    Journal of Plankton Research. 2008;31(3):287–300.

26. Hu C, Cannizzaro J, Carder KL, Muller-Karger FE, Hardy R.
    Remote detection of *Trichodesmium* blooms in optically complex coastal waters: Examples with MODIS full-spectral data.
    Remote Sensing of Environment. 2010;114(9):2048–2058.

27. Taylor IA, Preston J, Carboni E, Mather TA, Grainger RG, Theys N, et al.
    Exploring the Utility of IASI for Monitoring Volcanic SO2 Emissions.
    Journal of Geophysical Research: Atmospheres. 2018;123(10):5588–5606.